Journal of Molecular Liquids 376 (2023) 121400

Contents lists available at ScienceDirect

Journal of Molecular Liquids

journal homepage: www.elsevier.com/locate/molliq

Interface dielectric constant of water at the surface of a spherical solute

Mohammadhasan Dinpajooh [a], Dmitry V. Matyushov [b]

[a] Physical and Computational Sciences Directorate, Pacific Northwest National Laboratory, Richland, WA 99352, United States
[b] Department of Physics and School of Molecular Sciences, Arizona State University, PO Box 871504, Tempe, AZ 85287, United States

ARTICLE INFO

Article history:
Received 9 May 2022
Revised 30 January 2023
Accepted 4 February 2023
Available online 10 February 2023

Keywords:
Dielectric constant
Interface
Solvation
Polarization
Ewald sums
Molecular dynamics simulation
Quadrupole

ABSTRACT

Interface dielectric constant is used to quantify polar response of water interfacing a spherical solute. This interfacial parameter, affected by the interfacial structure within about two hydration layers, is fundamentally distinct from the bulk dielectric constant (a material property). Molecular dynamics simulations are used to extract the interface dielectric constant from fluctuation relations correlating the dipole moment of the interfacial layer with the medium electrostatics. For a probe ion, one has to calculate cross-correlations between the hydration shell dipole moment and the electrostatic potential, while cross-correlations between the shell dipole moment and the electrostatic field are required for a probe dipole. All protocols produce dielectric constants of water interfacing a nonpolar solute significantly below the bulk value. We analyze corrections imposed on the fluctuation relations by protocols using periodic boundary conditions with Ewald sums to compute electrostatic interactions. These corrections are insignificant for typical simulation protocols.

1. Introduction

Polar susceptibility of an interface has recently attracted much attention from theory [1–6] and experiment [7–10]. A consistent result from these efforts is that the response of the interfacial polar liquid and the corresponding interfacial dielectric susceptibility are substantially reduced compared to the bulk when probed in the direction perpendicular to the substrate. Only the response in the perpendicular direction could be tested experimentally so far. On the other hand, computer simulations allow probing polar response in both perpendicular and parallel directions to the dividing surface separating the liquid from the substrate. These studies have shown that the interfacial dielectric constant is highly anisotropic, thus becoming an axial tensor, with the parallel projection showing either the bulk-like behavior or polarity much exceeding that of the bulk [11–14].

Most simulations have been done for polar liquids in the slab geometry, when equations for the local dielectric susceptibility are significantly simplified [15,1]. The effective polarity of liquids interfacing solutes of more complex geometries is also of much interest to theories of solvation and interfacial polarization. Therefore, the polar response of water interfacing model spherical solutes [1,16,17], fullerenes [18], and proteins[19] has been quantified. In agreement with studies using slab geometry, the interface dielectric constant of water is reduced when probed either in the radial direction of a spherical solute or perpendicular to the protein surface [19]. The present study clarifies technical aspects of calculating the effective dielectric constant around spherical solutes by numerical simulations based on periodic boundary conditions[20] and Ewald sums to evaluate electrostatic interactions [21–24].

The analysis of simulations aimed at extracting the interface dielectric constant requires accounting for finite-size corrections [17] in the Ewald sums protocol applied to calculate electrostatic interactions [20]. Here, we provide an extended analysis of simulations of neutral Kihara solutes[16] and show that finite-size corrections are minor when applied to a thin hydration layer used to determine the interface dielectric constant. We also derive analytical expressions for the interface susceptibility and interface dielectric constant, including a full analysis of finite-size effects.

The article starts with reviewing the formalism for an effective, coarse-grained dielectric constant of the interface around a spherical solute, followed with the analysis of simulation trajectories including finite-size corrections. We analyze the dipolar and quadrupolar components of the interfacial polarization to show that the density of interfacial bound charge is strongly affected by quadrupolar polarization. The interfacial quadrupolar density cannot, however, be directly calculated because of the lack of invariance to the choice of the reference point for the molecular quadrupole of a dipolar molecule. One therefore has to rely on either the interfacial charge density or the interfacial dipole density to study the interface polarization. Dipolar density is sufficient to define the coarse-grained interface dielectric constant.

E-mail address: dmitrym@asu.edu (D.V. Matyushov)

https://doi.org/10.1016/j.molliq.2023.121400
0167-7322/

The analysis of interfacial response developed previously[25] and implemented here anticipates placing a small probe charge (linear response) at the center of a spherical solute. The need for finite-size corrections arises from the fact that the total charge of the simulation cell becomes nonzero when the probe charge is instantaneously placed at the solute. This difficulty is avoided when susceptibility in response to a point dipole is analyzed. The second part of the paper presents a new formalism to produce the interface dielectric constant from the response to a probe dipole. Consistent with the response to a probe charge, the interface dielectric constant is strongly reduced relative to the bulk.

2. Polarization of the interface

The microscopic electric field in a dielectric material is a sum of the field of external charges and the field of fluctuating bound (molecular) charge distributed with the charge density ρ_b. The external field in our model is produced by a small probe charge q placed at the center of a spherical solute. The Gauss theorem[26] defines the microscopic, instantaneous electric field $E_m(r)$ normal to the surface of the sphere with the radius r (Gaussian units)

$$4\pi r^2 E_m(r) = 4\pi(q + q_b(r)), \tag{1}$$

where $q_b(r)$ is the total bound charge within the r-sphere. Note that both $E_m(r)$ and $q_b(r)$ fluctuate as the system configuration changes. If the macroscopic Maxwell field $E(r) = q/(\epsilon r^2)$ is adopted to replace the microscopic electric field $E_m(r), q_b(r)$ gains a constant value independent of the sphere radius r

$$q_b = -q(1 - \epsilon^{-1}), \tag{2}$$

where ϵ is the bulk dielectric constant. The independence of q_b of the macroscopic radius makes one conclude that all bound charge must be accumulated within a microscopic interfacial region, where the microscopic field deviates from the macroscopic Maxwell field. Once accumulated in the microscopic region, the screening charge is constant for any macroscopic radius r outside of the charge accumulation region.

This observation can be directly proven by noting that the density of bound charge is equal[27,26] to the divergence of the vector field of medium polarization $\mathbf{P}^t$

$$\rho_b = -\nabla\cdot\mathbf{P}^t = -r^{-2}\partial_r(r^2P_r^t), \tag{3}$$

where $P_r^t = \hat{\mathbf{r}}\cdot\mathbf{P}^t, \hat{\mathbf{r}} = \mathbf{r}/r$ and radial symmetry was applied to the second equation. In dielectric theories, $P_r^t \propto E_0 = q/r^2$ is proportional to the vacuum field of the external charge E_0 and thus one finds from Eq. (3) $\rho_b = 0$. The density of bound charge vanishes in the parts of the dielectric where macroscopic electrostatics applies.

Given that there is no bound charge density in the bulk, dielectric theories collapse all interfacial bound charge to the surface charge at the dividing surface separating dielectrics with different dielectric properties [27,26]. Its position is not exactly specified on the molecular scale. To produce the dielectric screening charge as specified by Eq. (2), the region with $E_m(r) \neq E(r)$ has to be included within the dividing surface. The surface charge density is, in turn, related to the polarization discontinuity at the dividing surface [27].

Discontinuity of the polarization field at the dividing surface separating a continuum dielectric from a vacuum cavity yields the surface charge density $\sigma_n = -P_r^t(a+0)$, where a is the radius of the dividing surface. This result is derived by integrating the Maxwell equation

$$\nabla\cdot\mathbf{E} = -4\pi\nabla\cdot\mathbf{P}^t \tag{4}$$

between two closely separated spheres at $a-0$ and $a+0$. The result is

$$E_r(a+0) - E_r(a-0) = 4\pi\sigma_n. \tag{5}$$

If $E_r(a+0) = q/(\epsilon a^2)$ and $E_r(a-0) = q/a^2$, one arrives at the dielectric result in Eq. (2) with $q_b = 4\pi a^2\sigma_n$.

The microscopic distribution of bound charge is produced by taking the statistical ensemble average over the liquid configurations. The resulting $\langle\rho_b(r)\rangle$ around two nonpolar solutes (Kihara [16], see below, and fullerene C_{60}[18]) are shown in Fig. 1a. The water model is TIP3P for the Kihara solute and SPC/E for C_{60}. The threshold $\langle\rho_b(r)\rangle \simeq 0$ is reached outside of the hydration layer with the thickness $\delta \simeq 5-6$ Å, which corresponds to roughly two hydration shells. The polarization response is thus continuum-like, $\rho_b = 0$, outside of the second hydration shell.

The density of bound charge is oscillatory within the microscopic interfacial region. The first positive spike in Fig. 1a represents hydrogen atoms of water preferentially oriented toward the nonpolar solute carrying zero charge and interacting with water only through a surface Lennard-Jones (LJ) potential. The second positive maximum represents hydrogens in the second hydration shell, which are much more disordered, hence producing a broader peak. The bound charge density around the Kihara solute computed here is compared to the charge density (shifted horizontally) of SPC/E water around a neutral C_{60} fullerene (both water models are at $T = 298$ K) [18]. The basic arrangements of molecular charge around two types of neutral solutes are very similar. Putting a negative charge on the solute produces an electrostatic pull on the first-shell hydrogens and the release of dangling O–H bonds [28,29] directed toward the solute (blue line in Fig. 1a).

Fig. 1a confirms that the bound screening charge is accumulated within a microscopic interfacial region with the thickness $\simeq \delta$. The radius of the dielectric cavity a should be chosen to allow at least

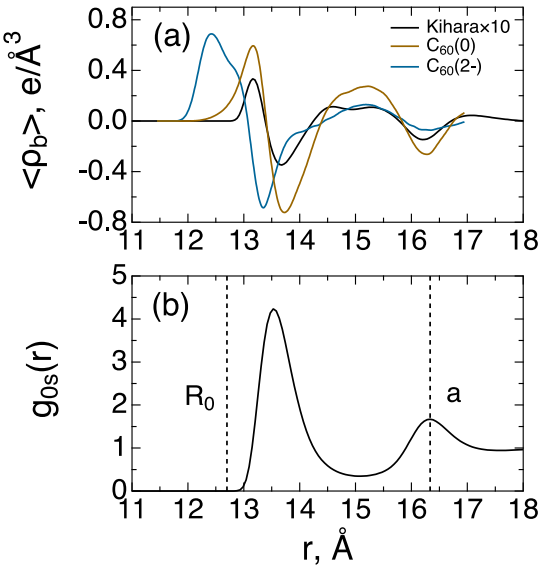

Fig. 1. (a) Average density of bound charge of TIP3P water ($T = 298$ K) $\langle\rho_b(r)\rangle$ around the Kihara solute with $R_{HS} = 10$ Å (black line). The brown line shows the bound charge density of SPC/E water around neutral C_{60} solute ($T = 298$ K) [18]. This curve is horizontally shifted by 6.9 Å to make the first maxima of two densities coincide. The charge density for the Kihara solute is multiplied by a factor of 10 to bring two functions to the same scale. The blue line shows the charge density around C_{60}^{2-} carrying the negative charge $q = -2e$. (b) Pair solute–solvent distribution function of water's oxygens around the Kihara solute. The vertical lines indicate the hard-sphere solute–solvent diameter $R_0 = 12.7$ Å and the position of the second density maximum identified with the cavity radius $a = 16.3$ Å.

partial accumulation of the screening charge within the divided surface. There is no exact criterion for positioning the dividing surface and we will associate a with the second maximum of the solute–solvent radial distribution function shown in Fig. 1b. Since the density maximum arises from preferential positions of water's oxygen atoms carrying negative partial charges, it corresponds to the second minimum of $\langle\rho_b(r)\rangle$ shown in Fig. 1a. As explained below, this choice minimizes the contribution of quadrupolar polarization to the surface charge density σ_n. The surface charge appears from collapsing the microscopic bound charge within the a-sphere to the dividing surface. Calculation of σ_n induced by an external probe charge or dipole is the goal of the formalism discussed below.

The comparison between neutral and charged C_{60} in Fig. 1a illustrates how the interfacial charge density is shifted by the pulling force from the solute charge. A change in ρ_b, induced by a probe multipole placed inside the solute, is quantified by the interfacial polar susceptibility, which is our primary goal. Theories of bulk dielectrics[27,26,30] represent changes in the scalar field ρ_b in terms of the vector field of dipolar polarization $\mathbf{P}$. In turn, the bulk dielectric constant is given by the variance of the dipole moment of the macroscopic sample and molecular quadrupoles do not directly contribute to it. They only affect local dipolar correlations entering the Kirkwood factor [31]. Is the same true for the interfacial polar response? To answer this question, we start by considering interfacial polarization in terms of individual contributions from dipolar and quadrupolar polarization components to the interfacial density of bound charge.

3. Dipolar and quadrupolar polarization

The superscript "t" in the polarization vector $\mathbf{P}^t$ in Eq. (3) specifies the total polarization field, which can be viewed as an (infinite) expansion in terms of multipolar densities of the liquid. If only the dipolar $\mathbf{P}$ and quadrupolar $\mathbf{Q}$ densities are included, one obtains[26]

$$\mathbf{P}^t = \mathbf{P} - \frac{1}{3}\nabla\cdot\mathbf{Q}, \tag{6}$$

where the densities of molecular dipoles $\mathbf{m}_j$ and quadrupoles $\mathbf{Q}_j$ are

$$\begin{aligned}\mathbf{P}(\mathbf{r}) &= \left\langle\sum_j \mathbf{m}_j\delta(\mathbf{r}-\mathbf{r}_j)\right\rangle,\\ \mathbf{Q}(\mathbf{r}) &= \left\langle\sum_j \mathbf{Q}_j\delta(\mathbf{r}-\mathbf{r}_j)\right\rangle.\end{aligned} \tag{7}$$

Here, the molecular quadrupole[26,32] $\mathbf{Q} = (3/2)\sum_k q_k\mathbf{r}_k\mathbf{r}_k$ is calculated relative to some arbitrary point chosen inside the solvent molecule[33] (see below); the sum runs over the atomic charges q_k with coordinates $\mathbf{r}_k$.

The statistically averaged radial projection $\langle P_r^t\rangle$ can be viewed as the derivative of the average radial dipole moment

$$M_r^t(r) = 4\pi\int_0^r dr\prime r^2\langle P_r^t\rangle \tag{8}$$

accumulated within the spherical region with the radius r around the solute. The average density of the bound charge directly follows from taking the statistical average in Eq. (3) and using the definition of $M_r^t(r)$ in Eq. (8)

$$\langle\rho_b\rangle = -(4\pi r^2)^{-1}\partial_r^2 M_r^t. \tag{9}$$

Integrating this equation, one obtains an expression for the radial shell dipole moment in terms of the charge density

$$M_r^t(r) = -4\pi\int_0^r dr\prime(r-r\prime)r\prime^2\langle\rho_b(r\prime)\rangle. \tag{10}$$

This shell dipole moment includes contributions from the radial dipole moment

$$M_r(r) = \left\langle\sum_{r_j<r}\hat{\mathbf{r}}_j\cdot\mathbf{m}_j\right\rangle \tag{11}$$

and from the corresponding density of quadrupoles[34]

$$M_r^t(r) = M_r(r) - \frac{4\pi}{3}r^2 Q_{rr}, \tag{12}$$

where Q_{rr} is the radial projection of the average quadrupolar density (Eq. (7)) in spherical coordinates.

Given that $\langle\rho_b(r)\rangle$ vanishes outside of the second hydration shell, integration in Eq. (10) does not extend beyond that microscopic region with the thickness $\delta\simeq 2\sigma_s$, where σ_s is the molecular diameter of the solvent. For large colloidal solutes with $a\gg 2\sigma_s$, one can assign a constant, mean-field value to $P_r^t = -P_n^t = -\hat{\mathbf{n}}\cdot\mathbf{P}^t$ inside the microscopic layer and put $\rho_b = 0$ at $r < R_0$ and $r > R_0+\delta$ (Fig. 1b). According to the standard rules of electrostatics [26,27], the projection of the polarization density is taken on the normal unit vector $\hat{\mathbf{n}}$ pointing outward from the solvent and toward the solute (Fig. 3).

From Eq. (8), one can write for $a\gg\delta$

$$M_r^t(a\to\infty)\simeq 4\pi\delta a^2\langle P_r^t\rangle. \tag{13}$$

Given $P_r^t = -P_n^t$, one obtains

$$M_r^t(a\to\infty) = -Q_{\rm int}\delta. \tag{14}$$

In this equation,

$$Q_{\rm int} = 4\pi a^2\langle P_n^t\rangle \tag{15}$$

is the total charge of the interface obtained by multiplying the surface charge density $\sigma_n = \langle P_n^t\rangle$ with the surface area of the dividing surface.

As is shown in Fig. 2, the dipole moment $M_r^t(r)$ saturates to a negative value $\simeq -0.6e\times$Å$\simeq -2.9$ D. Given $\delta\simeq 6$ Å (5 Å was reported in Ref. [35]), this value yields $Q_{\rm int}\simeq 0.1e$ in Eq. (9). The positive sign of $Q_{\rm int}$ is consistent with the positive potential $\phi_c = Q_{\rm int}/a$ inside an uncharged spherical cavity found in simulations of force-field water [36,37,35]. It reflects spontaneous interfacial polarization due to specific orientations of the water molecules [38,39]. The magnitude of $Q_{\rm int}$ estimated from Fig. 2 is consistent with the cavity potentials reported in the past [40].

In contrast to the total radial dipole $M_r^t(r)$, its dipolar component $M_r(r)$ saturates to a positive constant value $\simeq 25.7$ D

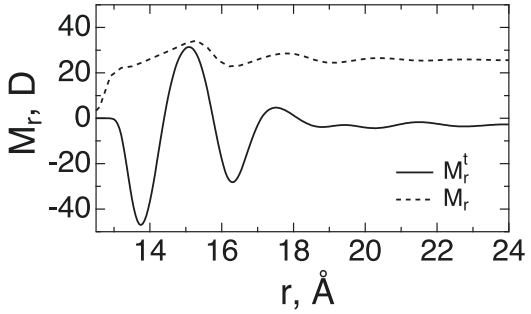

Fig. 2. Integrated radial dipole moment of the water shell $M_r^t(r)$ (Eq. (10), solid line) with the average density of bound charge of water $\langle\rho_b(r)\rangle$ around the Kihara solute with $R_{\rm HS} = 10$ Å. The saturation limit at large r is $M_r^t\simeq -2.9$ D. The dashed line refers to the integrated dipolar density $M_r(r)$ (Eq. (11)).

(Fig. 2). This implies that hydration shell dipoles are slightly tilted toward the bulk (Fig. 3), in opposite to the water–vapor interface where dipoles are tilted toward the vapor phase [34]. Dipoles tilted toward the bulk are seen from a reference point inside the solute as oxygen's negative charges (Fig. 3), yielding a negative interface charge. However, for each tilted dipole there is a positive hydrogen atom which is closer to the center of the solute than the negative oxygen. A compensation between two contributions leads to a positive net charge $Q_{\rm int}$ for TIP3P water. This compensation is strongly affected by the water model[37] and the solute–solvent interaction.

Despite its importance [2,34,41,35], the interfacial quadrupolar density cannot be calculated directly because of the lack of invariance of molecular quadrupole of a dipolar molecule in respect to the reference point [32,38]. This can be illustrated by taking water's quadrupole relative to the reference point at the oxygen atom. The radial quadrupolar density becomes

$$Q_{rr}(r) = q_H r_H^2 \left\langle \sum_i \delta(\mathbf{r}-\mathbf{r}_i) \sum_{k=1,2} P_2(\cos\theta_{ki}) \right\rangle, \tag{16}$$

where $q_H = 0.417e$ is the atomic charge of the hydrogen atom of TIP3P water and $r_H = 0.957$ Å is the length of the O–H bond. Further, $P_2(x)$ is the second Legendre polynomial and θ_{ki} $(k = 1, 2)$ are two angles between the O–H bonds of a water molecule and the radial direction established by the position of oxygen at $\mathbf{r}_i$.

Now assume that the reference point is shifted by the vector $\mathbf{b}$ along the symmetry axis of the water molecule. The quadrupolar density changes to

$$Q_{rr}\prime(r) = Q_{rr}(r) + 3mb\rho g_{0s}(r)\langle\cos^2\theta_r\rangle, \tag{17}$$

where $g_{0s}(r)$ is the solute-oxygen pair distribution function, ρ is the number density in the bulk, and θ_r is the angle between the O–H bond and the radial direction. If the traceless tensor is used for $\mathbf{Q}$ in Eq. (7), the expression $3\cos^2\theta_r$ in Eq. (17) is replaced with $3\cos^2\theta_r - 1$. The dependence on the reference point for the quadrupolar density disappears in the latter case for a point in the bulk, where $\langle 3\cos^2\theta_r - 1\rangle = 0$, but not in the interface. The interfacial quadrupolar polarization maintains its dependence on the choice of the reference point within the molecule even if traceless molecular quadrupole is adopted. The quadrupolar interfacial polarization is ill-defined when calculated from Eq. (7).

Fig. 4 illustrates the calculation of $Q_{rr}(r)$ based on Eq. (16). The radial quadrupolar density reaches a plateau consistent with the second term in Eq. (17). If this limit is scaled with $g_{0s}(r)$, one obtaines the dashed line in Fig. 4. The overall function $Q_{rr}(r)$ is thus dominated by the second term in Eq. (17) and cannot be unambiguously defined. This difficulty is, however, eliminated if Q_{rr} is calculated from M_r^t and M_r (green line in Fig. 4): one obtains $Q_{rr} \propto r^{-2}$ at large r (Eq. (12)). Both of these interface dipoles are well-defined and are not affected by an arbitrary choice of the reference point for higher molecular multipoles.

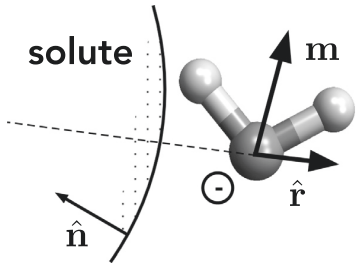

Fig. 3. Schematic drawing of spontaneous orientation of water dipoles $\mathbf{m}$ in the hydration shell of the Kihara solute with the radial direction indicated by $\hat{\mathbf{r}}$. The dipoles tilted toward the bulk produce an effective negative interface charge (marked with "–"). The charge is overall positive when both the dipolar and quadrupolar polarization components of the interfacial polarization are included (Fig. 2 and Eq. (12)). The unit normal vector $\hat{\mathbf{n}}$ perpendicular to the dividing surface points from the solvent toward the solute.

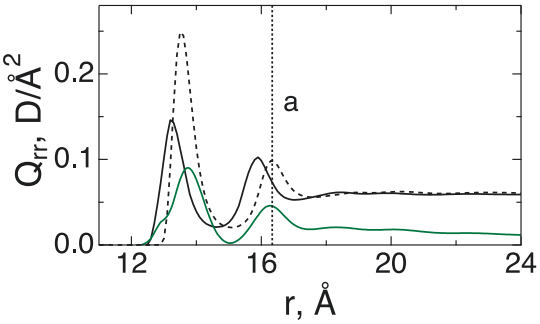

Fig. 4. Radial quadrupolar density Q_{rr} calculated according to Eq. (16) from MD trajectories for the Kihara solute in TIP3P water (solid line). The dashed line shows the second term in Eq. (17) in which $3mb\rho\langle\cos^2\theta_r\rangle$ is taken from the long-distance value of $Q_{rr}(r)$. The green solid line indicates Q_{rr} obtained from Eq. (12) with M_r^t and M_r shown in Fig. 2. The vertical dotted line indicates the dividing surface radius a.

To ensure that quadrupolar polarization does not contribute to the radial projection of the polarization vector field, the dividing surface is specified at the second minimum of $\langle\rho_b\rangle$ (Figs. 1 and 4) where the derivative in the second term in the following equation vanishes

$$P_r^t(r=a) = P_r - \frac{1}{3r^2}\partial_r(r^2 Q_{rr})|_{r=a} = P_r. \tag{18}$$

We now turn to the polarization field P_r induced at the dividing surface by an external charge or dipole.

4. Response to a charge

The focus of the formalism discussed here is not the overall interface charge, but rather the interface charge density σ_n induced by solute's electrostatics (Eq. (5)). The algorithm presented here aims to compute a coarse-grained, mean-field surface charge density characterizing the overall polarization induced in a microscopic region at the surface of the solute. With the assumption $\delta \ll a$, the target of this formalism is polar response of liquids at surfaces of colloidal particles with the size of a nanometer and larger (the Kihara solute studied here has the diameter of $\simeq 2.5$ nm). We start with considering the response to a single charge q placed at the solute's geometrical center, followed with the response to a point dipole. The contribution of the quadrupolar density to σ_n is neglected per Eq. (18): the induced surface charge density σ_n is viewed as arising solely from the interfacial dipolar polarization.

The surface charge density $\sigma_n = \langle P_n\rangle_q$ is obtained by projecting $\mathbf{P}$ on the surface normal $\hat{\mathbf{n}}$ pointing outward from the solvent (Fig. 3)

$$\langle P_n\rangle_q = \hat{\mathbf{n}}\cdot\langle\mathbf{P}\rangle_q. \tag{19}$$

The angular brackets $\langle\ldots\rangle_q$ denote an ensemble average in the presence of charge q. By performing a linear expansion of the statistical average in the interaction of charge q with the medium electrostatic potential ϕ_s, one gets the induced surface charge density

$$\Delta P_n = \langle P_n\rangle_q - \langle P_n\rangle_0 = -\beta q\langle\delta P_n\delta\phi_s\rangle_0, \tag{20}$$

where the spontaneous polarization component $\langle P_n\rangle_0$, if non-zero, is subtracted from the total. The statistical average $\langle\ldots\rangle_0$ denotes configurations in the absence of the solute charge $(q = 0)$ and

$\delta\phi_s = \phi_s - \langle\phi_s\rangle_0, \delta P_n = P_n - \langle P_n\rangle_0$ are deviations from the averages in the reference state. The electrostatic potential ϕ_s produced by the solvent is calculated at the position of the probe charge, which is the geometrical center of the solute in the present calculations. Note that binary correlations in the right-hand side of Eq. (20) calculated for the neutral solute, $\langle\dots\rangle_0$, must be equal to the same binary correlations calculated on configurations produced with a charged solute, $\langle\dots\rangle_q$, when linear response is adopted. This is because the structure of the interface is viewed as unperturbed by the solute–solvent electrostatics in linear response. Molecular dynamics (MD) simulations[16] support this assumption for relatively large Kihara solutes with the radius of ~ 1 nm studied here.

The induced surface polarization ΔP_n defines the linear surface susceptibility in response to the vacuum field E_{0n}

$$\Delta P_n = \chi_{0n} E_{0n}, \tag{21}$$

where, for spherical symmetry, one has $\hat{\mathbf{n}} = -\hat{\mathbf{r}} = -\mathbf{r}/r$ (Fig. 3)

$$E_{0n} = \hat{\mathbf{n}}\cdot\mathbf{E}_0 = \partial_r\phi_0|_{r=a}. \tag{22}$$

Here, $\phi_0 = q/r$ is the electrostatic (vacuum) potential of the charge q. From Eqs. (20) and (21), one obtains[25]

$$\chi_{0n} = \beta a^2\langle\delta P_n\delta\phi_s\rangle_0. \tag{23}$$

In this equation, δP_n is determined from calculating the dipole moment from a thin layer at the dividing surface $r = a$. One can instead make r a variable, which leads to oscillatory $P_n(r)$ and $\chi_{0n}(r)$ in the hydration shell. This difficulty applies to all attempts to define polar response at a specific spatial point in the interface [1,42], which also produced divergent dielectric constants for the longitudinal response in the slab geometry [43]. An algorithm around this difficulty[25] is to use a mean-filed, coarse-grained value of P_n characterizing the entire water shell within the microscopic region with the thickness δ. By taking a small increment $\Delta r = r - a \ll a$ in Eq. (8), one can write

$$P_n = -\frac{\Delta M_r}{\Delta V(r)} \simeq -\frac{1}{4\pi a^2}\frac{\Delta M_r}{\Delta r}, \tag{24}$$

where $\Delta V(r) \simeq 4\pi a^2\Delta r$ is the shell volume and M_r is calculated as the entire dipole moment within the r-sphere (Eq. (11)). From this equation and Eq. (23), one obtains the linear interface susceptibility as the slope of the cross-correlation between the radial shell dipole moment from Eq. (11) and the electrostatic potential of the medium calculated at the position of the probe charge

$$\chi_{0n} = -\frac{\beta}{4\pi}\frac{\Delta}{\Delta r}\langle\delta M_r\delta\phi_s\rangle_0. \tag{25}$$

The slope $\Delta/\Delta r$ in this equation is calculated from the dependence of $\langle\delta M_r\delta\phi_s\rangle_0$on r with $\Delta r = r - a$ taken beyond the dividing surface (see below).

The scalar parameter χ_{0n} is the coarse-grained susceptibility of the interface which delivers no information about the solvent polar response far from the dividing surface. Calculations of such distance-dependent susceptibilities carry little physical meaning since only the capacitance of a thin liquid film can be measured experimentally [7,10]. There is no spatial resolution in such measurements and both the experimental and simulation results fit well to the model of a layered capacitor combining the interfacial layer of thickness δ and the dielectric constant $\epsilon_{\rm int}$ and the bulk layer with the dielectric constant ϵ [42].

Calculations of the interface susceptibility through Eq. (25) anticipate that only the linear portion of $\Delta M_r \propto \Delta r$ is used to determine the slope (the assumption in Eq. (24) that the layer's volume is $\Delta V = 4\pi a^2\Delta r$ obviously fails when Δr is increased). This requirement poses an obvious challenge when used in numerical simulations. One wants a sufficiently large Δr to incorporate $\simeq 1-2$ layers of water beyond the radius a for sufficient statistics combined with $\Delta r \ll a$. Taken together, these conditions require sufficiently large solutes and correspondingly large simulation boxes. Implementing this algorithm in numerical simulations employing periodic boundary conditions and Ewald sums requires finite-size corrections considered next.

4.1. Finite-size corrections

We now apply the formalism outlined above to numerical simulations involving periodic boundary conditions and Ewald sums to calculate electrostatic interactions. A spherical solute is placed at the center of a cubic simulation cell with the length L. The cell is replicated by periodic boundary conditions to form a lattice bounded by a sphere of the radius R with the "tin-foil" condition of an infinite dielectric constant at the bounding sphere [20]. The solute carries no charge in its equilibrium state, which is assumed to be the reference state for the linear response perturbation theory. The ensemble average $\langle\dots\rangle_0$ over the statistical configurations in this state is specified with the zero subscript (Eqs. (20) and (25)).

When a small charge q is instantaneously added to the center of a spherical solute, the nuclei of the medium do not move during the addition (an analog of a spectroscopic vertical transition), but the image charges and the uniform background, with the charge density $\rho_0 = -q/L^3$ to neutralize q, are added instantaneously [23]. The energy of the simulation cell changes by

$$u = q\phi_s + \frac{q^2}{2}\xi. \tag{26}$$

Here, $\xi \simeq -2.837298/L$ is the electrostatic potential of the Wigner lattice of the central cell images (surrounded by a "tin-foil" boundary[44]). Additional finite-size corrections can be introduced for equilibrium free energies of ions to account for the fact that periodic polar media under-solvate the charge:[24] $\xi \to \xi(1-\epsilon^{-1})$ for a point charge[45] and correction terms depending on the ionic size for the electrostatic chemical potential of a finite-size ion [46,24].

The electrostatic potential of the solvent at the position of the probe charge is calculated in simulations employing periodic boundary conditions[20] through the Ewald potential $\psi(\mathbf{r})$

$$\phi_s = \sum_{i=1}^{N}\sum_{\alpha} q_{i\alpha}\psi(\mathbf{r}_{i\alpha}), \tag{27}$$

where $q_{i\alpha}$ are partial atomic charges with coordinates $\mathbf{r}_{i\alpha}$ within N solvent molecules; α runs over all partial charges within a given molecule. The Ewald potential is given as a sum of the real-space and reciprocal-space terms[20,21]

$$\psi(\mathbf{r}) = \frac{\mathrm{erfc}(\kappa r)}{r} + \frac{4\pi}{L^3}\sum_{\mathbf{k}\neq 0}\frac{1}{k^2}e^{-k^2/(4\kappa^2)+i\mathbf{k}\cdot\mathbf{r}} - \frac{\pi}{L^3\kappa^2}. \tag{28}$$

The decay parameter κ is typically chosen to be sufficiently large to eliminate the need to perform lattice sums in real space (the first term in Eq. (28)), $\mathbf{k}$ are the lattice vectors in reciprocal space.

The formalism used to arrive at Eqs. (23) and (25) needs to accommodate the field of the lattice of periodic images of the central ion when applied to simulation protocols based on Ewald sums [17]. The normal projection of the electric field at the dividing surface becomes

$$E_{0n} = q\partial_r\psi|_{r=a} = -\frac{q}{a^2}\zeta. \tag{29}$$

The parameter ζ in this equation provides the correction due to the lattice of images of the central ion

$$\zeta = \mathrm{erfc}(\kappa a) + \frac{2\kappa a}{\sqrt{\pi}}e^{-(\kappa a)^2} + \frac{4\pi a^2}{L^3}\sum_{\mathbf{k}\neq 0}\frac{1}{k}e^{-k^2/(4\kappa^2)}j_1(\kappa a), \tag{30}$$

where $j_1(x)$ is the spherical Bessel function of the first order[47] and the angular average over the dividing surface was used to simplify the final expression. Eq. (25) for the susceptibility becomes

$$\chi_{0n} = -\frac{\beta}{4\pi\zeta}\frac{\Delta}{\Delta r}\langle \delta M_r \delta\phi_s\rangle_0. \tag{31}$$

Fig. 5 plots $\zeta(a)$ from Eq. (30) for $\kappa = 6.4/L$ used in MD simulations of Kihara solutes in TIP3P water [16]. There is no significant correction for finite size effects for $a/L \leqslant 0.2$. The correction factor drops below unity with increasing size of the solute and approaches $\zeta \simeq 0.5$ when the size of the solute becomes equal to half of the simulation box. Lee and Singer[17] suggested an empirical approximation for the correction parameter

$$\zeta = 1 - (4\pi/3)(a/L)^3. \tag{32}$$

This simple function matches Eq. (23) very well for the protocol adopted in our simulations[16] (Fig. 5). It might appear that the parameter κ in Eq. (30) is irrelevant. However, the choice of κ does affect the correction parameter (Fig. 6) and the estimate by Eq. (32) is not always reliable. Nevertheless, the value $\kappa L = 6.4$ adopted in the simulation protocol (vertical dashed line in Fig. 6) provides nearly the lowest sensitivity of the correction factor to the solute size a. For a Kihara solute with the hard-sphere core R_{HS} equal to 10 Å (see below), the hard-sphere solute radius is $R_0 = 12.7$ Å[48] (Fig. 1b) and one finds $\zeta = 0.96$ for $a = R_0$ and $\zeta = 0.92$ for $a = 16.3$ Å as defined in Fig. 1b ($L = 60$ Å was used in simulations). The corrections arising from applying Ewald sums thus contribute about 8% of the calculated value of the susceptibility χ_{0n}.

From the interface susceptibility χ_{0n} in Eq. (31), one can define the effective dielectric constant of the interface [1,25]

$$\epsilon_{\rm int} = \left[1 - 4\pi\chi_{0n}\right]^{-1}. \tag{33}$$

This interface dielectric constant specifies the coarse-grained surface charge density σ_n and the boundary conditions for the discontinuity of the Maxwell electrostatic field at the dividing surface (Eq. (5)). The dielectric constant $\epsilon_{\rm int}$ enters the electrostatic boundary-value problem to calculate electrostatics in the void within a liquid dielectric [25]. It replaces the bulk dielectric constant of dielectric theories to account for the microscopic structure of the liquid interface, but should not be used to characterize screening of molecular charges by polar liquids [49,42].

Fig. 7 shows the analysis of simulation results for the Kihara solute with the hard-core radius $R_{HS} = 10$ Å and dipolar density for the water shell according to Eq. (11). The Kihara solute-water interaction energy $u_{0s}(r)$ combines the hard-sphere core with the radius R_{HS} with a soft Lennard-Jones (LJ) layer characterized by the LJ diameter σ_{0s} and the LJ energy ϵ_{0s}

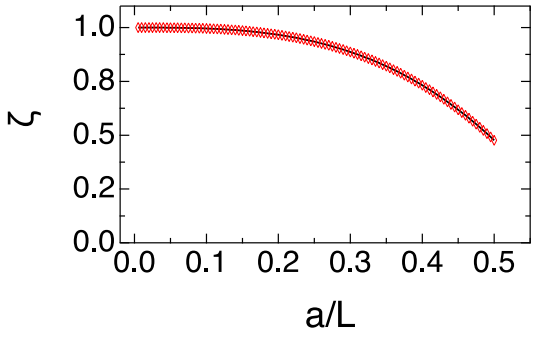

Fig. 5. Correction coefficient ζ in Eq. (30) vs a/L for $\kappa L = 6.4$ used in MD simulations (solid black line). Red points coinciding with the black line indicate the result of Eq. (32).

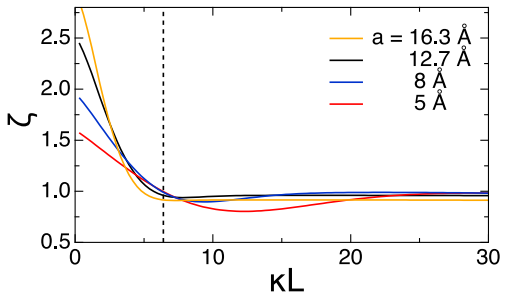

Fig. 6. Correction coefficient ζ in Eq. (30) vs κL for the values of the dielectric cavity radius a listed in the plot. The vertical dashed line indicates $\kappa L = 6.4$ adopted in MD simulations [25].

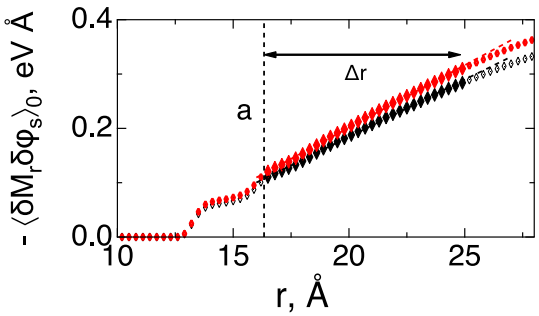

Fig. 7. Cross-correlation between the shell dipole moment M_r (Eq. (11)) and the medium electrostatic potential ϕ_s vs the distance r from the center of the solute (black open points). Open red points show the same correlation multiplied with ζ^{-1} (Eq. (30)). The cavity radius $a = 16.3$ Å is shown by the vertical dashed line. The filled points indicate the correlation data selected within the range $\Delta r \simeq 8.5$ Å and the dashed lines are the linear fits through the filled points to determine intrface susceptibilities χ_{0n} in Eqs. (25) (black) and (31) (red). The linear fits produce $\epsilon_{\rm int}$ equal to 5.5 (Eq. (25)) and 9.5 (Eq. (31)).

$$u_{0s}(r) = 4\epsilon_{0s}\left[\left(\frac{\sigma_{0s}}{r - R_{HS}}\right)^{12} - \left(\frac{\sigma_{0s}}{r - R_{HS}}\right)^{6}\right]. \tag{34}$$

The convenience of this potential for modeling solvation of large solutes is that it maintains a sufficiently steep solute–solvent repulsion while allowing to model partial surface dewetting and layering by modifying ϵ_{0s} [50].

The solute–solvent radial distribution function has its first peak approximately at the distance $R_{HS} + \sigma_{0s}$ from the solute center (Fig. 1b). The results shown in Fig. 7 are obtained at $\epsilon_{0s} = 3.7$ kJ/mol and $\sigma_{0s} = 3$ Å. Full wetting of the solute by TIP3P water is realized with these parameters [48].

MD simulations were done as described elsewhere [48]. Briefly, simulations were carried out at 298 K in the configuration of a single solute in a cubic box consisting of 6180–6650 TIP3P water molecules with the water density at 1.0 g/cm^3 after initial NPT equilibration. The production NVT runs were carried out for 200 ns with the time step of 2 fs. The simulation box length was 60 Å and the particle mesh Ewald method with the 12 Å cutoff distance was used for electrostatic interactions. The dielectric constants of bulk TIP3P and SPC/E water models were presented in a separate paper applying the algorithm of $k \to 0$ extrapolation in the polarization structure factors to avoid finite-size effects [51]. These bulk values are much larger than the interfacial dielectric constants presented here: $\epsilon = 94.28$ (TIP3P, $T = 300$ K) and $\epsilon = 70.95$ (SPC/E, $T = 300$ K).

The linear fit of $-\langle \delta M_r \delta\phi_s\rangle_0$, required to determine the slope in Eqs. (25) and (31) (red and black points in Fig. 7), was done for the

shell extending the distance $\Delta r = r - a \simeq 8.5$ Å beyond the cavity radius a (dashed vertical line in Fig. 7). This empirical choice of Δr leads to $\epsilon_{\rm int} \simeq 5.5$ in Eq. (25) and $\simeq 9.5$ in Eq. (31), when finite-size corrections are included.

When $\Delta r \simeq 10$ Å was applied to the analysis of neutral C_{60} in SPC/E water, $\epsilon_{\rm int}(T) \simeq 12 - 15$ was found in the range of temperatures $T \simeq 240 - 360$ K [18]. Further, when negative charge was added to C_{60} to create structural instability toward release of O–H bonds, $\epsilon_{\rm int}(T)$ increased to $20 - 25$. The range of numbers reported here is consistent with recent simulations of TIP3P water interfacing a planar substrate [52]. A careful analysis of the interfacial water structure revealed a small gap between water and the substrate. With the account of vacuum permittivity in the gap, the interfacial water layer was assigned the dielectric constant of $\simeq 17$.

5. Response to a dipole

The algorithm to evaluate the interface dielectric constant discussed here considers the water interface polarized by a radially symmetric electric field of the probe charge placed at the center of a spherical solute. This setup gives access to the longitudinal dielectric susceptibility[1,25,42]

$$\chi^L = (4\pi)^{-1}\left(1 - \epsilon_{\rm int}^{-1}\right). \tag{35}$$

The interface dielectric constant $\epsilon_{\rm int}$ can be associated in this case with the perpendicular dielectric constant $\epsilon_{\rm int} = \epsilon_\perp$ measured in the dielectric slab when an external field is applied perpendicular to the slab plane. Simulations of thin films of liquids (but not experiment) have additionally provided access to the dielectric response parallel to the slab planes [11–14], with the dielectric constant $\epsilon_\parallel$. The application of the external field parallel to the slab planes yields the transverse dielectric susceptibility

$$\chi^T = (4\pi)^{-1}\left(\epsilon_\parallel - 1\right). \tag{36}$$

These simulations have shown a significant anisotropy of the interfacial dielectric response with $\epsilon_\perp \ll \epsilon_\parallel$. One of the advantages of using the slab geometry is that two different geometries of the applied field, perpendicular and parallel to the slab surface, give access to, respectively, longitudinal and transverse susceptibilities, which refer to polar response in reciprocal space [53].

While the center charge induces the longitudinal polarization only, a probe dipole induces polarization including components of both longitudinal (L, irrotational, $\nabla \times \mathbf{P}_L = 0$) and transverse (T, solenoidal, $\nabla \cdot \mathbf{P}_T = 0$) symmetries [26,54]. The electrostatic chemical potential μ_d of a point dipole placed at the center of a spherical solute can be expressed in terms of microscopic, k-dependent longitudinal (L) and transverse (T) dipolar structure factors[53,55] $S^a(k), a = \mathrm{L,T}$ of the bulk liquid. The resulting expression is[56]

$$\mu_d = \sum_{a=\mathrm{L,T}} \frac{S^a}{g_K}\mu^a, \tag{37}$$

where $S^a = S^a(0)$ and $g_K = (S^L + 2S^T)/3$, the trace of the structure-factor tensor, is the Kirkwood factor of the polar liquid [31]. The terms μ^a are the reciprocal-space integrals of the L and T projections of the reciprocal-space electrostatic field of the dipole $\tilde{\mathbf{E}}_d$ with the corresponding structure factors

$$\mu^a = -\frac{3y}{8\pi}\int \frac{d\mathbf{k}}{(2\pi)^3}\left|\tilde{\mathbf{E}}_d^a\right|^2 S^a(k), \tag{38}$$

where $y = (4\pi/9)\beta\rho m^2$ is the standard parameter of dimensionless dipolar density appearing in dielectric theories [57,31].

Since we are interested in the limit of large colloidal solutes, the Fourier-transformed projections of the solute electric field decay on the scale of wavevectors a^{-1} for which the dipolar structure factors are nearly constant and can be approximated by their $k = 0$ values. Continuum limits $S^a(k) \to S^a(0)$ can be taken in the reciprocal-space integrals in Eqs. (37) and (38). The chemical potential for the dipole m_0 placed at the center of the solute becomes

$$\mu_d = -\frac{m_0^2}{a^3}\frac{yS^LS^T}{g_K}. \tag{39}$$

The reaction field [58] at the solute center is

$$R = -\partial\mu_d/\partial m_0 = \chi_d m_0. \tag{40}$$

It involves the susceptibility of the interface to the probe dipole

$$\chi_d = \frac{2y}{a^3}\frac{S^LS^T}{g_K}. \tag{41}$$

For dielectrically isotropic liquids in contact with the solute, one has $S^L = (\epsilon - 1)/(3y\epsilon), S^T = (\epsilon - 1)/(3y)$ and

$$\chi_d = \frac{1}{a^3}\frac{2(\epsilon - 1)}{2\epsilon + 1}. \tag{42}$$

This is the standard Onsager expression for the reaction field susceptibility [58].

If, alternatively, one applies $\chi^a = 3yS^a/(4\pi)$from Eqs. (35) and (36) to Eq. (39), one gets the reaction-field susceptibility in terms of the perpendicular and parallel components of the dielectric constant

$$\chi_d = \frac{2}{a^3}\frac{(\epsilon_\parallel - 1)(\epsilon_\perp - 1)}{2\epsilon_\parallel\epsilon_\perp - \epsilon_\perp - 1}. \tag{43}$$

This result reduces to the Onsager equation for the isotropic dielectric constant $\epsilon_\parallel = \epsilon_\perp = \epsilon$. In the opposite limit of strong anisotropy $\epsilon_\parallel \gg \epsilon_\perp$, the susceptibility turns to the longitudinal response (perpendicular component)

$$\chi_d = \frac{1}{a^3}\left(1 - \epsilon_\perp^{-1}\right). \tag{44}$$

From $\epsilon_\parallel \gg \epsilon_\perp$ obtained in simulations of interfacial water [11–14], the response of the microscopic interface to a dipole is mostly longitudinal and similar to that of an ion. This conclusion also follows from microscopic calculation of dipole solvation in dipolar liquids [59] suggesting that $\epsilon_\parallel \gg \epsilon_\perp$ should be a general property of polar liquid interfaces [14,60]. It is useful to note that the Onsager susceptibility (Eq. (42)) has been widely used[61–63,54] to analyze spectral solvatochromism. Dielectric anisotropy of the interface requires revision of the corresponding polarity parameters.

When a point dipole is placed at the center of a spherical cavity, the induced density of surface charge $\Delta P_n(\theta) = P_{n1}\cos\theta$ scales with the first-order Legendre polynomial of the polar angle θ relative to the direction of the dipole aligned with the z-axis of the laboratory frame. The reaction field (Eq. (40)) is given[54] in terms of the expansion coefficient P_{n1} as $R = -(4\pi/3)P_{n1}$. The linear perturbation theory allows one to express the reaction field in terms of the cross-correlation between fluctuating P_{n1} and the z-projection E_{sz} of the electric field of the medium at the center of the solute

$$R = -\frac{4\pi\beta m_0}{3}\langle\delta P_{n1}\delta E_{sz}\rangle_0. \tag{45}$$

The Legendre projection P_{n1} of the instantaneous polarization at the interface can be written as follows

$$P_{n1} = -\frac{3}{4\pi a^2}\sum_j(\hat{\mathbf{z}}\cdot\hat{\mathbf{r}}_j)(\hat{\mathbf{r}}_j\cdot\mathbf{m}_j)\delta(r_j - a). \tag{46}$$

Given spherical symmetry of the problem, one can represent the dipolar susceptibility in Eqs. (40) and (45) as

$$\chi_d = \frac{\beta}{3a^2}\frac{\Delta}{\Delta r}\langle \delta \mathbf{M}_r \cdot \delta \mathbf{E}_s \rangle_0, \tag{47}$$

where

$$\mathbf{M}_r = \sum_{r_j<r} \hat{\mathbf{r}}_j (\hat{\mathbf{r}}_j \cdot \mathbf{m}_j). \tag{48}$$

Eq. (47) suggests that the linear susceptibility of the hydration shell to the probe dipole can be calculated from the slope, with increasing thickness Δr, of the cross-correlation of the radial shell dipole moment $\mathbf{M}_r$ with the electrostatic field $\mathbf{E}_s$ produced by the medium at the solute center. From Eq. (44), one obtains

$$\epsilon_{\rm int} = \epsilon_\perp = \left(1 - a^3\chi_d\right)^{-1}. \tag{49}$$

The results of calculations of $\langle \delta \mathbf{M}_r \cdot \delta \mathbf{E}_s \rangle$ in Eq. (47) for the Kihara solute are shown in Fig. 8. The dashed straight line indicates the slope from the $\Delta r \simeq 8.5$ Å shell, with the result $\epsilon_{\rm int} = \epsilon_\perp \simeq 4.4$ in Eq. (49). This outcome is about twice below $\epsilon_{\rm int} \simeq 9$ calculated from the susceptibility in response to the charge field incorporating finite-size corrections (Fig. 7).

A disadvantage of the dipolar route to the interface dielectric constant is that the susceptibility $a^3\chi_d$ in Eq. (49) carries a weak $\propto a$ dependence on the cavity size a. Such a sensitivity to the selection of the effective cavity radius does not appear for the susceptibility to the charge field (Eq. (25)). However, the charge route requires Ewald-sum corrections for the electrostatic potential, which can be mostly neglected[64] in the calculation of the electrostatic field by the Ewald sums protocol. The dipolar route leading to Eq. (49) is based on Eq. (44), which follows from the assumption $\epsilon_\parallel \to \infty$ and might be inaccurate. Calculating two components, $\epsilon_\parallel$ and $\epsilon_\perp$, is not possible through a single susceptibility χ_d in Eq. (43).

A full understanding of the reasons behind the discrepancy between $\epsilon_{\rm int} \simeq 5-9$ for a central-symmetry charge probe and $\epsilon_{\rm int} = \epsilon_\perp \simeq 4$ for the dipolar probe is missing. The common acceptance of the bulk dielectric constant as a material property anticipates that the dielectric constant is independent of the symmetry of the probing external electric field. The arguments, going back to Ramshaw [65], show that specific linear combinations of the longitudinal and transverse susceptibilities eliminate the long-range, $\propto r^{-3}$, dipolar correlations and preserve only short-range correlations entering the Kirkwood factor and decaying on the length ℓ much shorter than the size of a macroscopic sample L. This prescription allows one to calculate the bulk dielectric constant as a material property insensitive to the sample shape and symmetry of the probing field. The separation of length scales is obviously not guaranteed for the interfacial polarization extending to the distance δ comparable to ℓ. The interface susceptibility is obviously not a material property as it depends on the solute–solvent interaction. Some dependence on the symmetry of the probing field might be maintained, contributing to the discrepancy between the charge and dipole routes used in the present calculations.

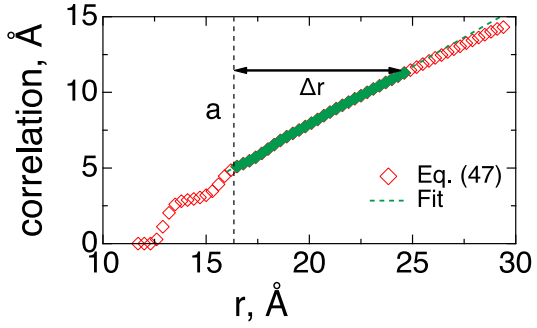

Fig. 8. Cross-correlation $(\beta a/3)\langle \delta \mathbf{M}_r \cdot \delta \mathbf{E}_s \rangle_0$ (red points, Eq. (47)) required to calculate the interface susceptibility in response to a probe dipole. The green points refer to $\Delta r = 8.5$ Å and the dashed green line refers to a linear fit through the filled points to determine the slope in Eq. (47). The fit yields the interface dielectric constant $\epsilon_{\rm int} = 4.4$ at $a = 16.3$ Å.

6. Discussion

Dielectric theories of polar materials have evolved from conventional boundary-value problems of macroscopic electrostatics to treat many ramifications of electrostatics on molecular scale in terms of one well-defined material property of the polar medium: the dielectric constant as reported by macroscopic dielectric experiments [57]. Electrostatic interactions are so ubiquitous on molecular and supramolecular length scales that it is difficult to pinpoint all limitations of this widely adopted approach. Two problems have received much attention in application to molecular phenomena in polar liquids: electrostatic solvation and screening of electrostatic interactions. Different extensions of the famous Born equation are used for the former. Limitations of this approach to solvation are well documented[66,23,48] although often not fully acknowledged because of a number of empirical schemes developed over the years for error corrections.

In contrast to ϵ, a material property [65], the interface dielectric constant $\epsilon_{\rm int}$ aims to capture the effect of the microscopic interfacial structure on polarization induced by a multipole placed at the solute (inside the dielectric cavity). The interfacial polarization is a vector field defining the scalar bound charge density (Eq. (3)) residing in a thin layer of about two molecular diameters at the solute surface. Accordingly, $\epsilon_{\rm int}$ quantifies the interfacial bound charge induced by the solute multipole. It replaces the bulk dielectric constant in the boundary-value problem seeking to calculate electrostatics inside a liquid void. The cavity radius a is chosen to make electrostatics continuum-like at $r > a$. However, electrostatics is not continuum-like inside the cavity, and this is reflected by $\epsilon_{\rm int} \neq \epsilon$.

The original route[25] to the interface susceptibility is amended here with corrections for periodic boundary conditions and Ewald sums used to calculate electrostatics. The correction within the standard Ewald sum protocol leads to minor modifications of $\epsilon_{\rm int}$ for typical simulation parameters. The response to a probe charge was extended here to interfacial response to a small point dipole. Both formalisms lead to $\epsilon_{\rm int} \simeq 4-9$ falling far below the bulk dielectric constant for water (ϵ(TIP3P) $\simeq 94$[51]). Even though the interface and bulk dielectric constants are often compared, they refer to quite distinct properties, interfacial for the former and bulk for the latter. The interface dielectric constant is sensitive to the interfacial structure and to the solute–solvent interaction, while bulk dielectric constant is insensitive to surface effects.

There is a long history of modeling the interfacial polar susceptibility with continuous functions of the distance into the bulk [67–70]. They are constructed to interpolate between $\epsilon_{\rm int}$ in a thin interfacial layer with the thickness δ and the bulk dielectric constant ϵ. While such models are convenient to use because of their well-defined mathematical properties [7], there is no physical reason to adopt such models as a fair representation of reality until direct measurements of the spatial extent of the interfacial polar structure become possible. The only measurement available so far is the capacitance of a thin liquid layer [7–10]. Both the laboratory and simulation results fit well to the model of a layered capacitor[42] combining a thin layer of thickness δ, characterized by $\epsilon_{\rm int}$, with a bulk-like layer carrying the dielectric constant ϵ. No

information beyond this separation into two distinct layers exists at the moment. This study presents a computational algorithm for ϵ_{int} in this layered model of the liquid film.

While the results for ϵ_{int} are robust and are in line with a number of recent simulation[2–5] and experimental[7–10] studies, one should avoid extrapolating ϵ_{int} reported here outside the scope of the boundary-value problem. The interface susceptibility ϵ_{int} applies to electrostatics produced by the interface in a void inside a polar liquid or to polarization of a thin film for which ϵ_{int} contributes to the film capacitance. Screening of charges in polar liquids involves an oscillatory potential of mean force at the distances between the charges comparable to the length of several solvent molecules [71–75,49]. The potential of mean force and microscopic screening cannot be characterized by a single scalar property [76], even though the screening potential reaches the standard dielectric result at large separations. In contrast to macroscopic dielectric theories, different electrostatic phenomena at the molecular scale require distinct effective polar susceptibilities.

The generic form of the density of bound charge around nonpolar solutes (Fig. 1a) suggests that a low value of the interface dielectric constant is a general and robust property of such interfaces. On the other hand, the overall interface charge is a result of opposite contributions from the dipolar and quadrupolar polarization components. In line with previous studies [33,35], we find that the inhomogeneous quadrupolar density in the interface is a major contributor to the interface charge and to the electrostatic potential produced by the solvent inside an uncharged cavity in the liquid.

Data Availability

The data that support the findings of this study are openly available at github.

Data availability

Data will be made available on request.

Declaration of Competing Interest

The authors declare that they have no known competing financial interests or personal relationships that could have appeared to influence the work reported in this paper.

Acknowledgements

This research was supported by the National Science Foundation (CHE-2154465). The supercomputer time was provided through Extreme Science and Engineering Discovery Environment (XSEDE) allocation MCB080071 and through ASU's Research Computing.

References

[1] V. Ballenegger, J.-P. Hansen, J. Chem. Phys. 122 (2005) 114711.
[2] D.J. Bonthuis, S. Gekle, R.R. Netz, Phys. Rev. Lett. 107 (2011) 166102.
[3] S. Mondal, S. Acharya, B. Bagchi, Phys. Rev. Res. 1 (2019) 033145.
[4] M.H. Motevaselian, N.R. Aluru, ACS Nano 14 (2020) 12761.
[5] P. Loche, C. Ayaz, A. Wolde-Kidan, A. Schlaich, R.R. Netz, J. Phys. Chem. B 124 (2020) 4365.
[6] S. Mondal, B. Bagchi, J. Chem. Phys. 154 (2021) 044501.
[7] O. Teschke, G. Ceotto, E.F. De Souza, Chem. Phys. Lett. 326 (2000) 328.
[8] O. Teschke, G. Ceotto, E.F. de Souza, Phys. Rev. E 64 (2001) 011605.
[9] O. Teschke, E.F. de Souza, Phys. Chem. Chem. Phys. 7 (2005) 3856.
[10] L. Fumagalli, A. Esfandiar, R. Fabregas, S. Hu, P. Ares, A. Janardanan, Q. Yang, B. Radha, T. Taniguchi, K. Watanabe, G. Gomila, K.S. Novoselov, A.K. Geim, Science 360 (2018) 1339.
[11] R. Renou, A. Szymczyk, G. Maurin, P. Malfreyt, A. Ghoufi, J. Chem. Phys. 142 (2015) 184706.
[12] S. Mondal, B. Bagchi, J. Phys. Chem. Lett. 10 (2019) 6287.
[13] P. Loche, C. Ayaz, A. Schlaich, Y. Uematsu, R.R. Netz, J. Phys. Chem. B 123 (2019) 10850.
[14] M.H. Motevaselian, N.R. Aluru, J. Phys. Chem. Lett. 11 (2020) 10532.
[15] H.A. Stern, S.E. Feller, J. Chem. Phys. 118 (2003) 3401.
[16] M. Dinpajooh, D.V. Matyushov, J. Chem. Phys. 145 (2016) 014504.
[17] M.-S. Lee, S.J. Singer, J. Phys. Chem. B 125 (2021) 2360.
[18] S.M. Sarhangi, M.M. Waskasi, S.M. Hashemianzadeh, D. Matyushov, J. Phys. Chem. B 123 (2019) 3135.
[19] S. Seyedi, D.V. Matyushov, Chem. Phys. Lett. 713 (2018) 210.
[20] M.P. Allen, D.J. Tildesley, Computer Simulation of Liquids, Clarendon Press, Oxford, 1996.
[21] S.W. DeLeeuw, J.W. Perram, E.R. Smith, Proc. R. Soc. London Ser. A 373 (1980) 27.
[22] F. Figueirido, G.S. Del Buono, R.M. Levy, J. Chem. Phys. 103 (1995) 6133.
[23] G. Hummer, L.R. Pratt, A.E. Garcia, J. Phys. Chem. 100 (1996) 1206.
[24] P.H. Hünenberger, J.A. McCammon, J. Chem. Phys. 110 (1999) 1856.
[25] D.V. Matyushov, J. Chem. Phys. 140 (2014) 224506.
[26] J.D. Jackson, Classical Electrodynamics, 2nd ed., Wiley, New York, 1975.
[27] L.D. Landau, E.M. Lifshitz, Electrodynamics of Continuous Media, Pergamon, Oxford, 1984.
[28] G.L. Richmond, Chem. Rev. 102 (2002) 2693.
[29] J.-J. Velasco-Velez, C.H. Wu, T.A. Pascal, L.F. Wan, J. Guo, D. Prendergast, M. Salmeron, Science 346 (2014) 831.
[30] H. Fröhlich, Theory of Dielectrics, Oxford University Press, Oxford, 1958.
[31] G. Stell, G.N. Patey, J.S. Høye, Adv. Chem. Phys. 48 (1981) 183.
[32] C.G. Gray, K.E. Gubbins, Theory of Molecular Liquids, Fundamentals, Vol. 1, Clarendon Press, Oxford, 1984.
[33] M.A. Wilson, A. Pohorille, L.R. Pratt, J. Chem. Phys. 90 (1989) 5211.
[34] L. Horváth, T. Beu, M. Manghi, J. Palmeri, J. Chem. Phys. 138 (2013) 154702.
[35] C.C. Doyle, Y. Shi, T.L. Beck, J. Phys. Chem. B 123 (2019) 3348.
[36] H.S. Ashbaugh, J. Phys. Chem. B 104 (2000) 7235.
[37] R.C. Remsing, T.T. Duignan, M.D. Baer, G.K. Schenter, C.J. Mundy, J.D. Weeks, J. Phys. Chem. B 122 (2018) 3519.
[38] T.L. Beck, Chem. Phys. Lett. 561-562 (2013) 1.
[39] T. Dufils, C. Schran, J. Chen, A.K. Geim, L. Fumagalli, A. Michaelides (2022), arXiv:2211.14035.
[40] D.V. Matyushov, Biomicrofluidics 13 (2019) 064106.
[41] S. Parez, M. Předota, M. Machesky, J. Phys. Chem. C 118 (2014) 4818.
[42] D.V. Matyushov, J. Phys. Chem. B 125 (2021) 8282.
[43] A. Schlaich, E.W. Knapp, R.R. Netz, Phys. Rev. Lett. 117 (2016) 048001.
[44] B.R.A. Nijboer, T.W. Ruijgrok, J. Stat. Phys. 53 (1988) 361.
[45] F. Figueirido, G.S. Del Buono, J. Phys. Chem. 101 (1997) 5622.
[46] G. Hummer, L.R. Pratt, A.E. García, B.J. Berne, S.W. Rick, J. Phys. Chem. B 101 (1997) 3017.
[47] M. Abramowitz, I.A. Stegun (Eds.), Handbook of Mathematical Functions, Dover, New York, 1972.
[48] M. Dinpajooh, D.V. Matyushov, J. Chem. Phys. 143 (2015) 044511.
[49] S. Seyedi, D.R. Martin, D.V. Matyushov, J. Phys.: Condense Matter 31 (2019) 325101.
[50] A.D. Friesen, D.V. Matyushov, Chem. Phys. Lett. 511 (2011) 256.
[51] T. Samanta, D.V. Matyushov, J. Mol. Liq. 364 (2022) 119935.
[52] F. Deißenbeck, C. Freysoldt, M. Todorova, J. Neugebauer, S. Wippermann, Phys. Rev. Lett. 126 (2021) 136803.
[53] P. Madden, D. Kivelson, Adv. Chem. Phys. 56 (1984) 467.
[54] D.V. Matyushov, Manual for Theoretical Chemistry, World Scientific Publishing Co. Pte. Ltd., New Jersey, 2021.
[55] T. Fonseca, B.M. Ladanyi, J. Chem. Phys. 93 (1990) 8148.
[56] D.V. Matyushov, J. Chem. Phys. 120 (2004) 7532.
[57] C.J.F. Böttcher, Theory of Electric Polarization, Vol. 1: Dielectrics in Static Fields (Elsevier, Amsterdam, 1973)
[58] L. Onsager, J. Am. Chem. Soc. 58 (1936) 1486.
[59] D.V. Matyushov, J. Chem. Phys. 120 (2004) 1375.
[60] J.-F. Olivieri, J.T. Hynes, D. Laage, J. Phys. Chem. Lett. 12 (2021) 4319.
[61] E. Lippert, Z. Electrochem. 61 (1957) 962.
[62] E.G. McRae, J. Phys. Chem. 61 (1957) 562.
[63] N. Mataga, T. Kubota, Molecular Interactions and Electronic Spectra, Marcel Dekker, New York, 1970.
[64] D.V. Matyushov, J. Chem. Phys. 155 (2021) 114110.
[65] J.D. Ramshaw, J. Chem. Phys. 66 (1977) 3134.
[66] B. Roux, H.-A. Yu, M. Karplus, J. Phys. Chem. 94 (1990) 4683.
[67] P. Debye, L. Pauling, J. Am. Chem. Soc. 47 (1925) 2129.
[68] B.E. Conway, J.O. Bockris, I.A. Ammar, Trans. Farad. Soc. 47 (1951) 756.
[69] L.S. Palmer, A. Cunliffe, J.M. Hough, Nature 170 (1952) 796.
[70] P.J. Stiles, J.B. Hubbard, R.F. Kayser, J. Chem. Phys. 77 (1982) 6189.
[71] S.E. Huston, P.J. Rossky, J. Phys. Chem. 93 (1989) 7888.
[72] A.A. Rashin, J. Phys. Chem. 93 (1989) 4664.
[73] D. Trzesniak, A.-P.E. Kunz, W.F. van Gunsteren, ChemPhysChem8 162 (2007).
[74] C.J. Fennell, A. Bizjak, V. Vlachy, K.A. Dill, J. Phys. Chem. B 113 (2009) 6782.
[75] Y. Luo, W. Jiang, H. Yu, A.D. MacKerell, B. Roux, Farad. Disc. 160 (2013) 135.
[76] F. Jiménez-Ángeles, K.J. Harmon, T.D. Nguyen, P. Fenter, M. Olvera de la Cruz, Phys. Rev. Res. 2 (2020) 043244.